Heterodyne dual-polarization epi-detected CARS microscopy for chemical and topographic imaging of interfaces

Wolfgang Langbein,[1, a)] David Regan,[1] Iestyn Pope,[1] and Paola Borri[2, b)]
[1)] *Cardiff University School of Physics and Astronomy, The Parade, Cardiff CF24 3AA, United Kingdom*
[2)] *Cardiff University School of Biosciences, Museum Avenue, Cardiff CF10 3AX, United Kingdom*

(Dated: 21 May 2018)

Coherent Raman Scattering (CRS) has emerged in the last decade as a powerful multiphoton microscopy technique offering chemically-specific label-free imaging in real time with high three-dimensional spatial resolution. Many technical realizations of CRS microscopy have been proposed to remove, suppress, or account for the non-resonant background in the nonlinear susceptibility which complicates spectral analysis and reduces image contrast. Here, we demonstrate coherent anti-Stokes Raman scattering microscopy using a dual-polarization balanced heterodyne detection in epi-geometry (eH-CARS), providing background-free chemically-specific image contrast for nanoparticles and interfaces, shot-noise limited detection, and phase sensitivity. We show the sensitivity and selectivity of eH-CARS in comparison with forward CARS and stimulated Raman scattering (SRS) on polystyrene beads in agarose gel. As an important biologically-relevant application, we demonstrate eH-CARS imaging of individual lipid bilayers with high contrast and topographic sensitivity.

I. INTRODUCTION

The exploitation of nonlinear light-matter interaction has resulted in the development of multi-photon microscopy techniques over the past decades, exhibiting three-dimensional (3D) spatial resolution afforded by the nonlinearity, creating signal only in the focus volume where high intensities are reached. Especially promising for imaging in cell biology are non-invasive label-free techniques which avoid the sample treatment and artifacts associated with staining protocols, and are additionally not limited by fluorophore photo-bleaching and related cyto-toxicity. Among those, coherent Raman scattering (CRS) is particularly interesting owing to its chemical specificity, i.e. its ability to provide distinct contrasts of endogenous biomolecules on the basis of their chemical composition. CRS uses the interference between two short laser pulses (called Pump and Stokes) with different carrier frequencies to coherently drive molecular vibrations using the intensity beat at the frequency difference. The resulting Raman scattered light from all bonds in the focal volume coherently interferes. Such coherent signal enhancement compared to spontaneous Raman has enabled high acquisition speeds for chemically-specific live cell imaging applications [1–3].

A common implementation of CRS is to detect the frequency up-shifted Raman scattering of the higher excitation frequency (Pump), called coherent anti-Stokes Raman scattering (CARS). This signal detection is free from excitation background, since the CARS optical frequency ν_{CARS} is spectrally well separated from the frequency of the exciting pump (ν_{P}) and Stokes (ν_{S}) pulses, following the relation $\nu_{\mathrm{CARS}} = 2\nu_{\mathrm{P}} - \nu_{\mathrm{S}}$. Detecting the CARS intensity, the signal is proportional to the modulo square of the detected field, and thus proportional to the modulo square of the non-linear CRS susceptibility. Through the modulo square, the vibrationally resonant and non-resonant part of the complex non-linear

[a)] Electronic mail: langbeinww@cardiff.ac.uk
[b)] Electronic mail: borrip@cardiff.ac.uk

CRS susceptibility interfere, giving rise to an asymmetric spectral lineshape for a resonant response. The non-resonant part also causes a background reducing image contrast for microscopy applications. The CRS susceptibility is actually the quantity of interest, which is proportional to the local material composition, and needs to be retrieved. When acquiring the CARS intensity over a wide spectral range, it is possible to retrieve the phase of the susceptibility [4–7]. However, this requirement limits the imaging speed, prompting the development of various methods to suppress the influence of the non-resonant background in the detected signal. Assuming an isotropic non-resonant background, e.g. in a liquid, the background contribution has a given polarization direction, and can be suppressed by detecting only the cross-polarized intensity [8]. Assuming a background dominated by a spatially homogeneous material, the background signal has a defined emission direction [9,10], which can be excluded from the detection (i.e. a dark-field approach). Furthermore, since the non-resonant response is temporally instantaneous, it can be removed by temporal filtering [11,12]. All these methods however remove a part of the CARS signal, and thus decrease the detected information content. By measuring two vibrational frequencies at the same time, as in dual/differential CARS [13,14] or using frequency modulation FM-CARS [15], the non-resonant background can also be suppressed while allowing for high speed acquisition.

Alternatively to detecting the CARS intensity, one can use an interferometric detection to measure the CARS field directly in amplitude and phase, thus retaining its full information content [16–18]. In this way, one can directly isolate the imaginary part of the complex susceptibility, which is given by the resonant response only, and is similar to the signal measured in spontaneous Raman scattering. However, achieving interferometric stability between the signal and the reference beams is challenging.

Detection of the CRS signal at the frequency of the Pump or Stokes fields provides such an interferometric detection intrinsically, and is called stimulated Raman scattering (SRS). The fixed phase relation between the excitation beam and the signal provides an amplitude change proportional to the imaginary part of the CRS susceptibility, and a phase modulation proportional to the real part. Therefore, simply detecting the transmitted Pump or Stokes intensity allows to measure the imaginary part, which is containing the resonant response only. However, the excitation fields have typically $10^4 - 10^6$ times higher amplitude than the CRS field, so that the resulting relative intensity changes are of the order $10^{-4} - 10^{-6}$, which are overwhelmed by fluctuations of the transmitted excitation intensity. Practical SRS implementations therefore use high-frequency (1-10 MHz) modulation of the amplitude of the non-detected excitation field, which modulates the signal accordingly, and a lock-in detection[19–21]. This allows suppression of slower fluctuations due to classical laser noise, microphonics, and sample inhomogeneities. However, SRS detected in this way is not completely free from background, and is affected by nonlinear transient absorption and scattering which can give rise to artifacts [22]. Nonlinear (multi-photon) absorption results in an amplitude variation similar to SRS. Non-linear scattering induced by one of the beams and experienced by the other, either via cross phase modulation (including the real part of the CRS susceptibility) or via photo-thermal effects, changes the angular distribution of the transmitted beam that is converted into an intensity variation by aperture clipping in the detection path.

As a further step toward the development of the ideal CRS detection free from background and artifacts, we report here on a multimodal SRS/CARS microscope featuring a novel CARS interferometric, dual-polarization heterodyne detection scheme in epi-geometry with balanced diode detection, providing background-free chemically-specific image contrast, shot-noise limited detection, and phase sensitivity. Notably, using a reference not passing via the sample, the epi signal phase provides direct topographic information on the axial position of the sample with nanometer precision. A back-to-back comparison between SRS, forward-detected intensity CARS (F-CARS), and epi-detected heterodyne CARS (eH-CARS) is shown on a set of polystyrene beads in agarose gel. A biologically-relevant application example is then presented, showing label-free imaging of single lipid bilayers with high contrast and phase sensitivity.

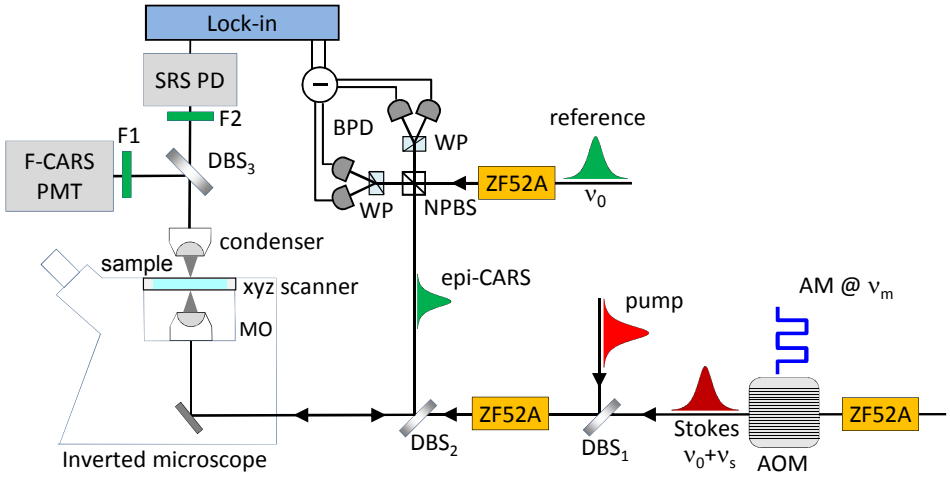

FIG. 1. Sketch of the multimodal SRS/F-CARS/eH-CARS microscope. Stokes pulses are amplitude-modulated at ν_m and radio-frequency shifted at ν_s using an AOM. Spectral focussing is applied via H-ZF57A glass blocks. Pump and Stokes are coupled via dichroic beamsplitters (DBS) into an inverted microscope. F-CARS is detected in transmission using a bandpass filter (F1) and a photomultiplier (PMT). SRS is detected using a bandpass filter F2 and a resonant photodiode (PD), and filtered at ν_m by a lock-in amplifier. eH-CARS is collected in epi-geometry and combined with an reference pulse by a non-polarizing beam-splitter (NPBS), polarization split by Wollaston-prism (WP) and detected by pairs of balanced photodiodes (BPD).

II. HETERODYNE EPI-DETECTED CARS

The eH-CARS microscopy technique we present here features a number of differences compared to previous realizations of heterodyne CARS [17,18]. Specifically, in our set-up (see Fig. 1 and details in Sec. VI) we have implemented an external reference beam, and a heterodyne CARS detection in epi-geometry with a balanced photodiode detector.

In order to understand these differences, let us recall that in heterodyne CARS the interference between a reference field and the CARS field is detected. The reference field has to be overlapped with the CARS field both in its spatial mode, and its temporal structure. Incoherent background, e.g. from fluorescence, or room light, is rejected, and does not affect the noise since the reference power can be chosen to dominate this background. Heterodyne detection is achieved by applying a frequency shift between signal and reference fields, providing a linear phase change of the interference, resulting in a beat which can be detected in amplitude and phase by a dual-channel lock-in amplifier. Previous works [17,18] used a reference beam combined into the same spatial mode as Pump and Stokes beam, and scanned together across the sample. This allows one to mode match signal and reference independent of beam scanning and collected mode quality, and to use forward detection employing a simple condenser lens.

This scheme however does not allow to use direct balanced detection, as only one beam intensity is measured. Notably, direct balanced detection is important to suppress classical noise of the reference, e.g. due to laser instabilities, or transmission inhomogeneities of the reference beam. Implementing an indirect balanced detection using a separate measurement of the reference intensity, as done e.g. for SRS with fibre laser sources[23], can reach the shot noise limit only if the resulting additional shot noise of the reference and the influence of transmission inhomogeneities can be neglected.

The choice of reference power in these previous heterodyne CARS configurations [17,18] was dictated by the requirement to minimize classical noise, while superseding detector noise and CARS intensity noise, in order to reach a shot-noise limited detection dominated by the reference. In practice, this resulted in reference powers of 1-100 nW and using a photomultiplier (PMT) for detection because of its low dark noise. However PMTs have quantum efficiencies lower than photodiodes (PDs) and suffer from amplification excess

noise.

We also note that using a reference collinear with the excitation measures all CRS generated, including the multiply scattered forward CRS, while using an external reference selects the back-scattered CARS only and rejects multiply scattered signal, similar to optical coherence tomography.

Since heterodyne detection directly determines the phase of the signal and can distinguish resonant from non-resonant responses, one might wonder what is the benefit of an additionally epi detection. In some applications the sample geometry and thickness excludes forward detection scattering, as for example in live non-transparent animal imaging [20]. In this case the detected signal is actually multiple-scattered forward CRS signal. The epi-detected heterodyne CARS recently reported in [24] refers to this case. On the other hand, when considering optically thin samples, such as nano-particles [25] or lipid bilayers [26] in which multiple scattering can be neglected, epi-detected CARS is intrinsically different from forward CARS, and is due to single scattering by sub-wavelength structures in the first-order susceptibility, i.e. the refractive index, or in the third-order susceptibility. For simple sample structures, this allows one to use the phase of the signal to determine the axial position with interferometric precision down to the nanometer range, as we demonstrated recently for single nanoparticles using electronically-resonant four-wave mixing [27].

With our eH-CARS technique, we address here this regime, allowing one to exploit the suppression of the signal from the bulk by epi detection, and using the phase to distinguish resonant from non-resonant responses and/or to determine the axial position of the object.

In the following we give a description of our eH-CARS set-up. Pump, Stokes and reference beams of about 150 fs duration at $\nu_L = 80$ MHz repetition rate are provided by a Ti:Sa pulsed laser source which is frequency-doubled to pump an Optical Parametric Oscillator (OPO) resulting in a tuneable signal output in the wavelength range 490-750 nm, and a corresponding idler in the range 930-2500 nm. To drive vibrational resonances in the CH-stretch region around 3000 cm^{-1}, the Ti:Sa fundamental beam at 820 nm wavelength was used as Pump, the tunable OPO idler at around 1080 nm was used as Stokes, and the OPO signal at around 660 nm was used as reference beam, which is phase- and wavelength-locked to the generated CARS field through the phase-preserving chain in the OPO [18].

Since typical vibrational resonances in condensed matter have coherence times in the picosecond range, we used the technique of spectral focussing to optimize the spectral selectivity of the excitation without loss of pulse energy. Spectral focusing is achieved by applying an equal linear chirp to pump and Stokes pulses, hence creating a constant instantaneous frequency difference (IFD) between them which selectively drives a vibrational excitation of interest. The spectral resolution is then given by the Fourier-limit of the temporal envelop of the chirped pulses which can be elongated to a few picoseconds. This approach allows us to tune the IFD within the spectral width of the pulses by simply adjusting their relative time delay, and thus to perform CARS spectroscopy without tuning the laser wavelength[28,29]. As previously demonstrated, a simple and efficient control of the linear chirp of Pump and Stokes pulses is obtained when they travel through glass blocks of known group-velocity dispersion [28,30]. We used here H-ZF52A and SF57 glass blocks of selected lengths for this purpose, and a motorized delay line in the Pump beam path to tune the IFD (see Sec. VI). Importantly, the reference pulse is also chirped by glass blocks to acquire the same linear chirp as the CARS signal at the point of the non-polarizing beam splitter (NPBS), and travels through a motorized delay line, in order to provide spectral and temporal overlap with the CARS field, allowing for heterodyning. This chirp is calculated assuming that the generated CARS signal at the sample has the same chirp as Pump and Stokes pulses, and taking into account the additional group velocity dispersion that the signal accrues during propagation from the sample to the NPBS, which is mostly due to the microscope objective and tube lens. The home-built instrument control software calculates the required glass lengths, using the known dispersion of the glass blocks, and the approximate equivalent glass combinations for objective and tube lens. The glass lengths are then set automatically by inserting selected glass blocks of given lengths into the beam path, and the pump and reference delays are adjusting accordingly. Total glass lengths used are typically 10-30 cm. More details are given in Sec. VI

For heterodyne detection, the Stokes beam was frequency up-shifted by the radiofrequency

$\nu_s = 77\,\mathrm{MHz}$ using an acousto-optic modulator (AOM) driven at ν_s. Pump and Stokes pulses are recombined by the dichroic beamsplitter DBS1, sent onto a commercial inverted microscope stand through a second dichroic beamsplitter DBS2, and focussed onto the sample by a high numerical aperture (NA) microscope objective. Pump and Stokes beams are horizontally polarized prior entering the microscope. The sample can be positioned and moved with respect to the focal volume of the objective by scanning an xyz sample stage with nanometric position accuracy.

eH-CARS is collected in epi-geometry by the same focussing objective used in excitation, reflected by DBS2 and recombined in the NPBS with the reference beam which is linearly polarized to have equal horizontal and vertically polarized fields. The resulting interference between the CARS and reference fields is separated by Wollaston prisms (WP) into horizontal and vertical polarization components, and detected by a balanced photodiodes (BPD) using the photo-current difference between the two interferometer arms. As mentioned, the interference of the epi-detected CARS with a reference outside the sample allows us to use PDs with high quantum efficiency and a balanced geometry to reject the classical noise of the reference, and to reach the shot noise limit.

Heterodyning is achieved using the CARS field frequency shift of $-\nu_s = -77\,\mathrm{MHz}$, resulting from its proportionality to the complex conjugate Stokes field. The interference with the reference is then detected at the beat note $\nu_L - \nu_s = 3\,\mathrm{MHz}$ using a dual-input dual-channel lock-in amplifier (ZI HF2), providing amplitude and phase components for both polarizations.

In the same set-up, we implemented SRS and conventional forward-CARS (F-CARS) detection for direct comparison. For SRS, the Stokes beam was amplitude modulated by the AOM, driven with a square wave amplitude modulation of frequency $\nu_m = 2.5\,\mathrm{MHz}$. F-CARS and SRS are collected by a 1.34 NA oil condenser in transmission geometry. A dichroic beamsplitter DBS3 reflects the F-CARS signal and transmits the Pump and Stokes beams. F-CARS is spectrally selected by a band-pass filter F1 and detected by a photomultiplier. SRS in the form of stimulated Raman loss is measured on the Pump beam, selected by the short-pass filter F2, and detected as an intensity modulation at $\nu_m = 2.5\,\mathrm{MHz}$ via a PD and a dual phase lock-in amplifier (ZI HF2), taking the in-phase component of the SRS modulation.

III. COMPARING EH-CARS, F-CARS AND SRS ON POLYSTYRENE BEADS

Three-dimensional eH-CARS, SRS and F-CARS measurements on polystyrene beads of $3\,\mu\mathrm{m}$, $1\,\mu\mathrm{m}$ and $0.2\,\mu\mathrm{m}$ diameter embedded in a 2% agarose gel are shown in Fig. 2 as in-plane (xy) and axial (xz) images. Corresponding lateral (x) and axial (z) line cuts through the bead center are shown in Fig. 3. Measurements were taken at an IFD of $3060\,\mathrm{cm}^{-1}$, resonant to the aromatic CH vibrational resonance of polystyrene. Pump and Stokes beams were linearly polarized along the x-axis at the sample. Forward detected SRS and CARS show background signal from the surrounding agar, which reduces image contrast and limits the visibility of the $0.2\,\mu\mathrm{m}$ diameter beads. In F-CARS this contribution is larger than in SRS since both the resonant and non-resonant parts of the third-order susceptibility of water contribute to the F-CARS intensity. In SRS, only the resonant part contributes and manifests as a signal which increases with increasing wavenumber toward the water OH stretching resonance around $\sim 3200\,\mathrm{cm}^{-1}$ (see Fig. 4). Note that in the SRS data shown, 1 mV signal corresponds to a relative modulation of the Pump transmission of about 3×10^{-6}, so that the relative modulation measured is about 3×10^{-4} for the $3\,\mu\mathrm{m}$ PS bead, and 2×10^{-5} for the $0.2\,\mu\mathrm{m}$ bead. The SRS noise is $1.5 \times 10^{-8}/\mathrm{rtHz}$, close to the estimated shot noise of $1.1 \times 10^{-8}/\mathrm{rtHz}$ for 2.8 mA photocurrent. This corresponds to 3.5×10^{-7} for the 500Hz bandwidth used at 1 ms pixel dwell time for the data in Fig. 2.

Notably, SRS and F-CARS show some image artifacts, although due to the high NA of the collection, the scattering induced artefacts in SRS are small. These originate from temperature dependent lensing (photothermal effect) and intensity dependent lensing (Kerr effect) [22] known to give rise to a background in SRS. The observed distortions in F-CARS

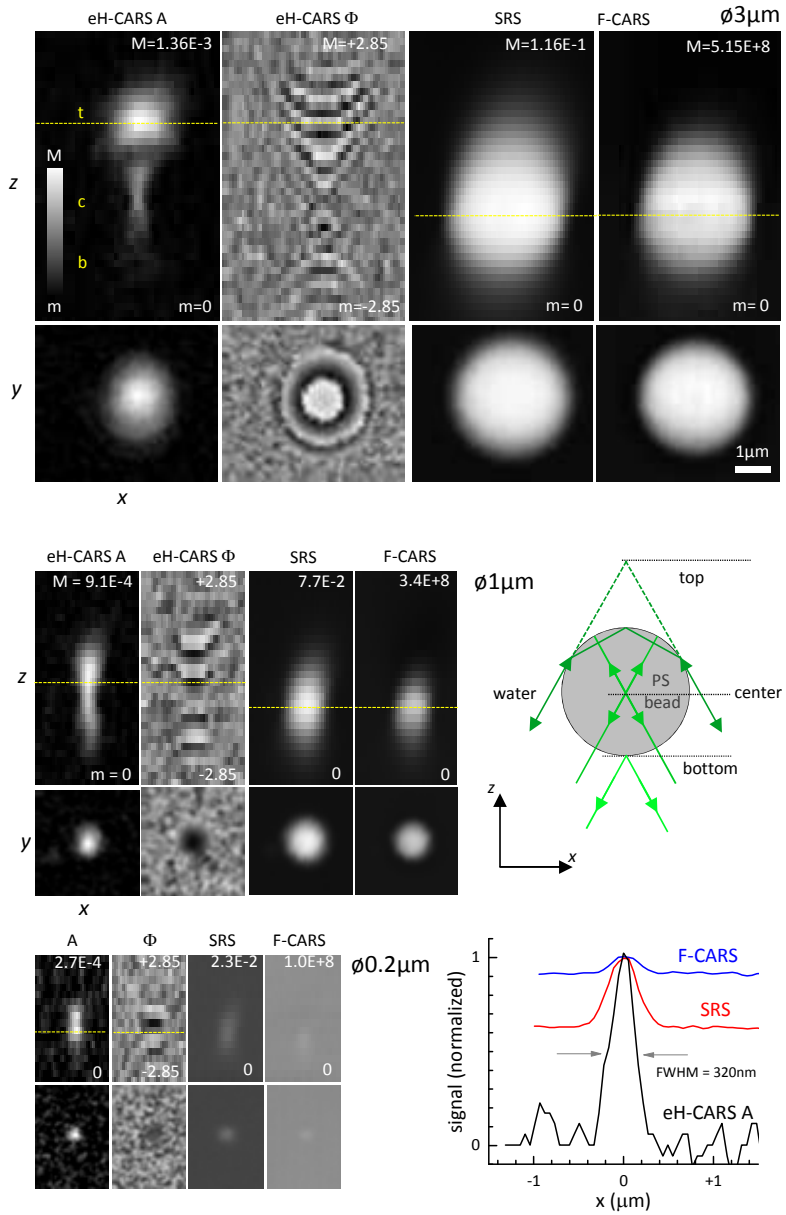

FIG. 2. eH-CARS amplitude (A) and phase (Φ), SRS, and F-CARS on polystyrene beads of 3 μm (top), 1 μm (middle) and 0.2 μm (bottom) diameter in agar, at an IFD of 3060 cm^{-1}. Axial (xz) images and corresponding in-plane (xy) images across the beads (see yellow lines) are shown. Grey scales from m (black) to M (white) as indicated. Values are in units of photoelectrons/sec at the PMT cathode for F-CARS, volts for eH-CARS amplitude (A) and SRS, and radians for the eH-CARS phase (Φ). The sketch illustrates the ray path on a large bead, giving rise to three eH-CARS maxima (see text). The graph shows normalized signals along the x-axis in the center of the 0.2 μm bead. See Sec. VI for more details.

are mostly due to shadowing effects of the water contribution near the bead edges [13] (see e.g. F-CARS z line-cuts in Fig. 3) .

Fig. 5 exemplifies these effects, by showing the negative contrast of the bead in F-CARS at 3090 cm^{-1} due to the interference between PS and water signal, and a SRS signal of a few percent of the resonant SRS signal, when Pump and Stokes beams are out of time overlap (Stokes arriving about 3 ps before pump), hence no longer driving a vibrational resonance. Looking at the SRS in-phase and in quadrature components, we find that this signal has

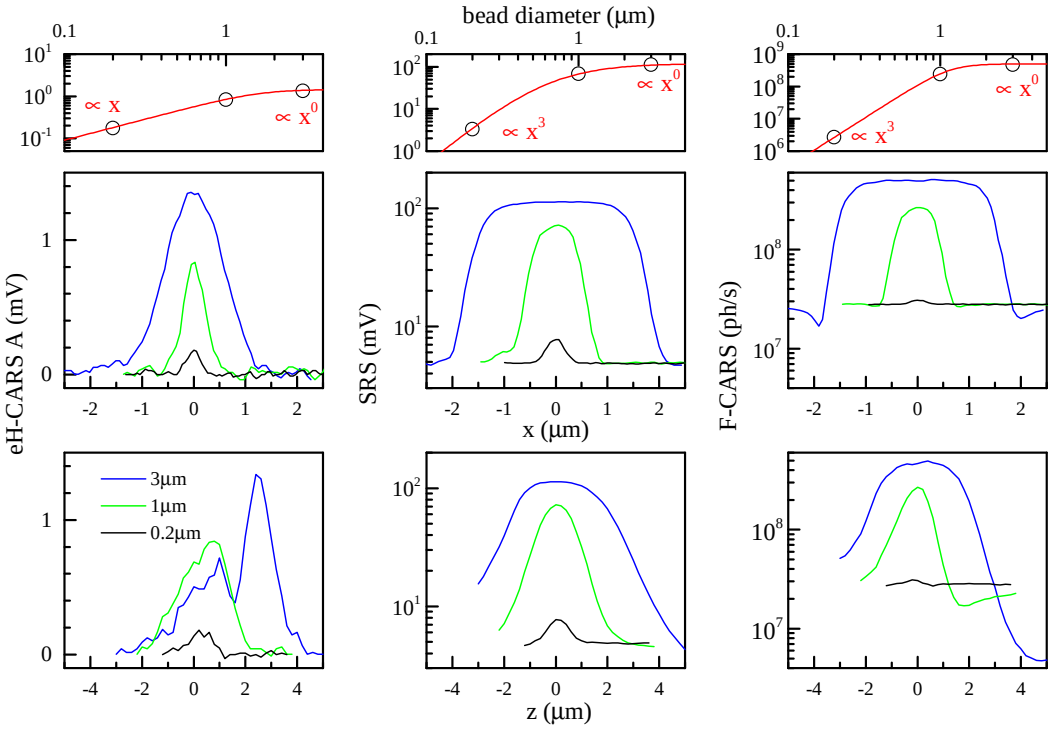

FIG. 3. Lateral (x) and axial (z) cuts of epi-detected heterodyne CARS amplitude (A), SRS, and forward-detected CARS intensity, through the center of polystyrene beads of 3 μm (blue lines), 1 μm (green lines) and 0.2 μm (black lines) diameter, resulting from the data shown in Fig. 2. The top panels plot the difference between the signal at the bead and the surrounding medium versus bead diameter (symbol), together with lines showing trends as indicated.

similar amplitudes in these components, showing that the signal is about 45 degrees phase shifted. Such a phase shift is expected for a photothermal signal which has a response time, given by the cooling dynamics of the focal volume, similar to the SRS modulation period of 400 ns. The differential contrast structure of the SRS Q is attributed to a remaining spatial modulation of the Stokes by the AOM. This modulation, which is along the vertical in Fig. 5, creates an SRS Q signal proportional to the vertical spatial derivative of the SRS I signal, and is thus pronounced at the edges of the PS bead. Conversely, eH-CARS shows maximum contrast free from the water contribution (due to the forward directionality of CARS emission from bulk media) and is resolved in amplitude and phase components, with shot-noise limited detection (see also Fig. 9).

Interestingly, eH-CARS exhibits a peculiar axial dependence, which is most evident for larger beads (see Fig. 2 and Fig. 3) with a maximum amplitude above the bead top interface. This pattern can be understood as a combination of signals due to steps in the first and third-order susceptibility at the bead surface, and is sketched in Fig. 2. Moving the focus from bottom to top, we first find a signal where the focus is at the bottom agar/bead interface. At that position, there is a step in the third-order susceptibility providing an epi-CARS contribution. If we call $\bar{\tilde{\chi}}$ the third-order susceptibility normalized to the glass susceptibility [5], we find that the imaginary part of $\bar{\tilde{\chi}}$ for PS on resonance at 3060 cm^{-1} is about 10, and the real part is about 2. Water instead has an imaginary part of about 0.4 and a real part around 1, so that the step magnitude in $\bar{\tilde{\chi}}$ is about 10. Moreover, the field reflection coefficient at the water / PS interface is about 8%, using the refractive indices of 1.33 for water and 1.58 for PS, which is reflecting the CARS field generated in the agar. This first signal is rather weak, and can best seen for the 3 μm bead in Fig. 2. Moving the focus up, the next point of interest is the focus in the center of the bead. In this case, the signal is dominated by CARS generated in the focus at the center of the bead, and

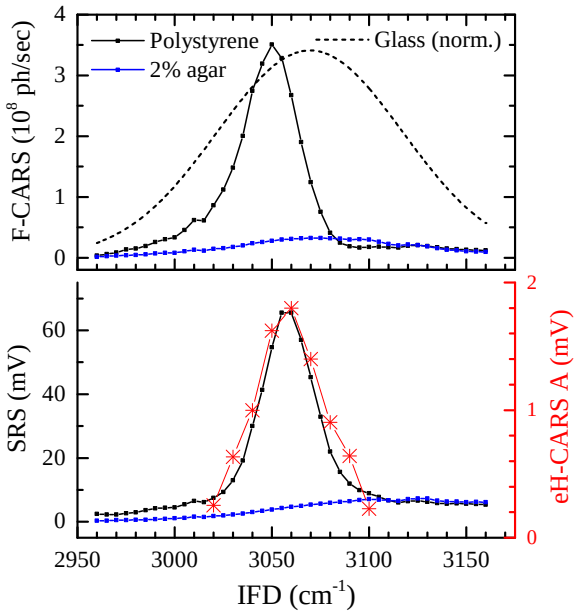

FIG. 4. Spectrally-resolved F-CARS and SRS in the center of a 1 μm diameter PS bead (black squares) and in the agar close to the bead (blue squares), as indicated. Spectra are obtained by changing the delay time between Pump and Stokes pulses and in turn the IFD. The normalized non-resonant response measured in glass, varying with the Pump-Stokes temporal overlap, is shown as dotted line. An eH-CARS amplitude spectrum on the PS bead, taken at the reference delay adjusted for best overlap for each IFD, is given in red.

reflected at the top surface. The shape of the signal in the xz plane is also suggestive of a focus, with the reflected field mode best overlapping with the reference when focussing into the center. Moving the focus further up, we find a minimum and then a broad region just above the bead featuring the strongest signal. This region is interpreted as the position of the virtual focus when the refraction by the bead is focussing the excitation onto the top internal surface, where the CARS field created inside the bead is reflected at a high angle of incidence, providing a high reflectivity and thus a strong signal. Importantly, due to the coherent detection, the fields due to these various mechanisms interfere. The nature of the interference depends on the relative phase of the signals which is given by the propagation phase and the phase of $\tilde{\bar{\chi}}$ or of the step in $\tilde{\bar{\chi}}$. One can clearly observe destructive interference between the three types of signals as dark lines. Even for the 0.2 μm bead, the signal shows an elongated shape with a weak double peak structure, evidence for this interference. Interestingly, the propagation phase changes the absolute phase of the signal, as can be seen in the eH-CARS phase, specifically clear for the 3 μm bead. Beyond these qualitative considerations, an in-depth understanding of these behaviors would require one to model the eH-CARS fields in a full Maxwell solver, which is beyond the scope of this paper.

Fig. 3 also compares the bead size dependence of the measured signals, scaling as D^3 for small diameters (D) in SRS and in F-CARS (for resonant parts below the non-resonant part of $\tilde{\bar{\chi}}$ the F-CARS intensity is dominated by the interference term with the non-resonant contribution, scaling as D^3), and saturating toward a constant value for diameter much larger than the focal volume. eH-CARS amplitude shows an almost linear D dependence, due to its sensitivity to surface/interface effects.

The spectra of eH-CARS, SRS, and F-CARS for the 1 μm bead are given Fig. 4. The intensity-detected F-CARS spectrum has the typical partly-differential lineshape due to the interference between the resonant and non-resonant parts of the CRS susceptibility. The SRS spectrum instead is free from non-resonant CRS, and shows a Raman-like shape with a dominating PS peak at 3060 cm^{-1} and a broad tail from the water resonance increasing towards higher IFD. Notably, the eH-CARS amplitude spectrum is similar to the SRS

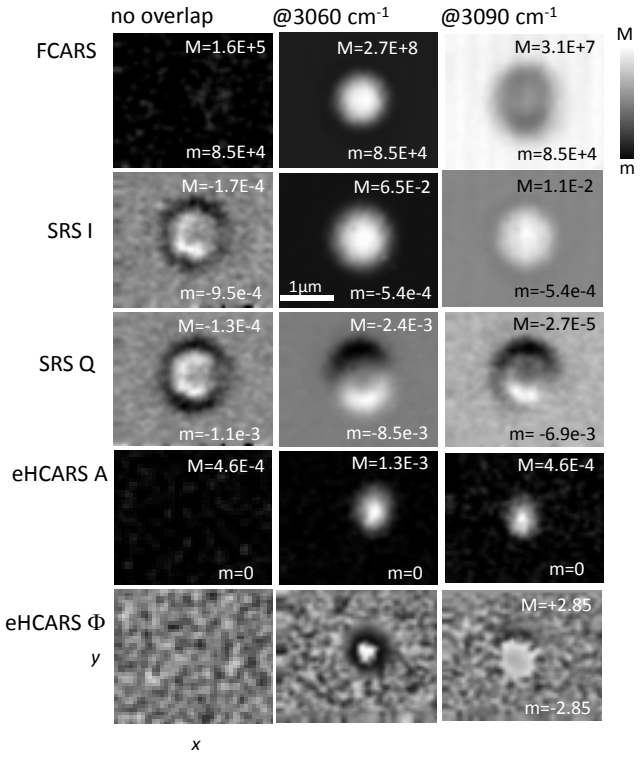

FIG. 5. Comparison between in plane (xy) images of F-CARS, SRS and eH-CARS amplitude and phase measured on a 1 μm diameter PS in agar. F-CARS and SRS are equatorial cuts, while eH-CARS is shown at the axial plane of maximum signal, slightly above the equatorial plane as shown in Fig. 2. Measurements are shown at the indicated IFD and when Pump and Stokes were out of time overlap, with the Pump arriving 3 ps after the Stokes. Both in-phase (SRS I) and in-quadrature (SRS Q) components are shown.

spectrum, having a peak at the PS resonance. This has likely two reasons. Firstly, there is no background contribution from the bulk agar in epi detection. Secondly, regarding the signal due to the step in $\bar{\tilde{\chi}}$, the difference between the PS and water $\bar{\tilde{\chi}}$ is measured, in which the non-resonant component of $\bar{\tilde{\chi}} \approx 3$ in PS [31] is partially removed by the non-resonant $\bar{\tilde{\chi}} \approx 1$ of water, thus decreasing the non-resonant contribution to the eH-CARS amplitude spectrum.

Having the dual polarization balanced detection, we found the eH-CARS to be dominantly polarized along the linear polarization direction of the Pump and Stokes, with the cross-polarized components having an amplitude less than 10% of the co-polarized component. One example of polarization resolved data on a 1 μm PS bead is shown in Fig. 6. We can see that the cross-polarized component has a node across the center of the bead, orthogonal to the linear excitation polarization. In this signal, polarization mixing can occur both in the excitation and in the signal due to the reflection at interfaces at non-normal incidence. Again, a more detailed understanding will require a modelling with a full vectorial Maxwell solver.

IV. PLANAR SINGLE LIPID BILAYERS

After having introduced our eH-CARS set-up and characterized its performance on polystyrene beads, let us here showcase its application to an important biophysical sample, namely a single lipid bilayer. Synthetic lipid membrane bilayers have been investigated for several decades to study lipid-lipid and lipid-protein interactions [32]. They serve as model

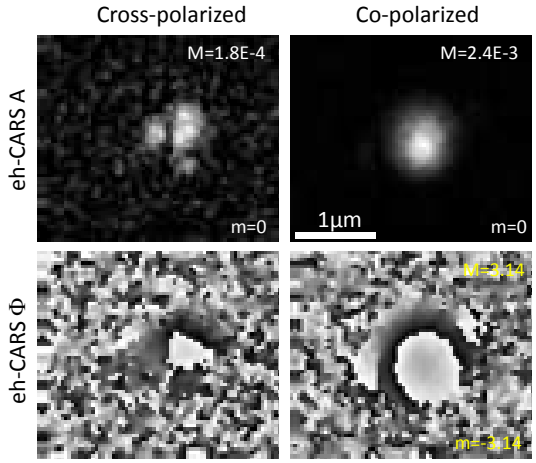

FIG. 6. Polarization resolved eH-CARS amplitude and phase measured on a 1 μm diameter PS in agar at 3050 cm^{-1}. Linear excitation polarization (horizontal), and co- and cross-polarized detection. In-plane (xy) images of eH-CARS at the axial plane of maximum signal.

systems to aid our understanding of the heterogeneous organization of cellular membranes and in the investigation of many processes including protein segregation in lipid domains, membrane protein function, drug-receptor interactions, and transmembrane transport. Understanding the chemical composition and structure of lipid bilayers with high sensitivity and spatial resolution is thus very important, yet technically challenging. Fluorescence microscopy is a valuable contact-free method, however, labeling phospholipids might lead to significant changes in their molecular shape and physicochemical properties, which may influence lipid spatial distribution, lipid dynamics, and functioning of the membrane [33]. Photobleaching of the labels also limits the quantitative analysis of fluorescence intensities. In that context, CRS microscopy provides a useful chemically sensitive label-free tool to investigate lipid membranes non-invasively and quantitatively in their native state, also applicable to living cells beyond model systems.

Since the coherent signal enhancement in CRS compared to spontaneous Raman relies on the constructive interference of the scattered light from all identical bonds in the focal volume, detection of a single 2D lipid bilayer, as compared to a 3D volume, pushes CRS microscopy to its sensitivity limits [1]. Using an intensity-based single-frequency CARS detection, and a low pulse repetition rate (20 times reduced compared to our system) to allow for higher peak powers (and thus CARS intensities) for a given average power, Li *et al.* [26] showed images of lipid domains in single supported bilayers without labeling, where vibrational contrast was generated by the molecular packing density difference between heterogeneous ordered/disordered lipid mixtures. They showed that epi-detection greatly improves contrast compared to forward detection, by eliminating the non resonant background from bulk water. However, by measuring the CARS intensity, the CARS phase was not accessible, and the signal was interpreted in terms of density ratios of CH_2 groups.

Here we demonstrate phase-sensitive eH-CARS image acquisition on a similar single lipid bilayer (Fig. 7), without the need for laser repetition rate reduction. The sample consists of a single lipid type (1,2-dipentadecanoyl-*sn*-glycero-3-phosphocholine- $DC_{15}PC$) deposited onto a planar glass substrate in order to form regions with single and double bilayers (see Sec. VI). To characterize the thickness of these regions, we used a quantitative differential interference contrast (qDIC) image analysis [25,34]. DIC microscopy measures the difference of the transmitted optical phase between two points in the sample plane, spatially separated by an amount (the shear) typically comparable with the optical resolution. Based on this principle, we can derive the spatial distribution of the optical phase which for lipid bilayers of known refractive index can in turn be used to calculate their thickness. For this analysis, we acquire the qDIC contrast image I_c defined as $I_c = (I_+ - I_-)/(I_+ + I_-)$ where $I_\pm$ are the transmitted intensities for opposite DIC phase offsets. The differential phase is

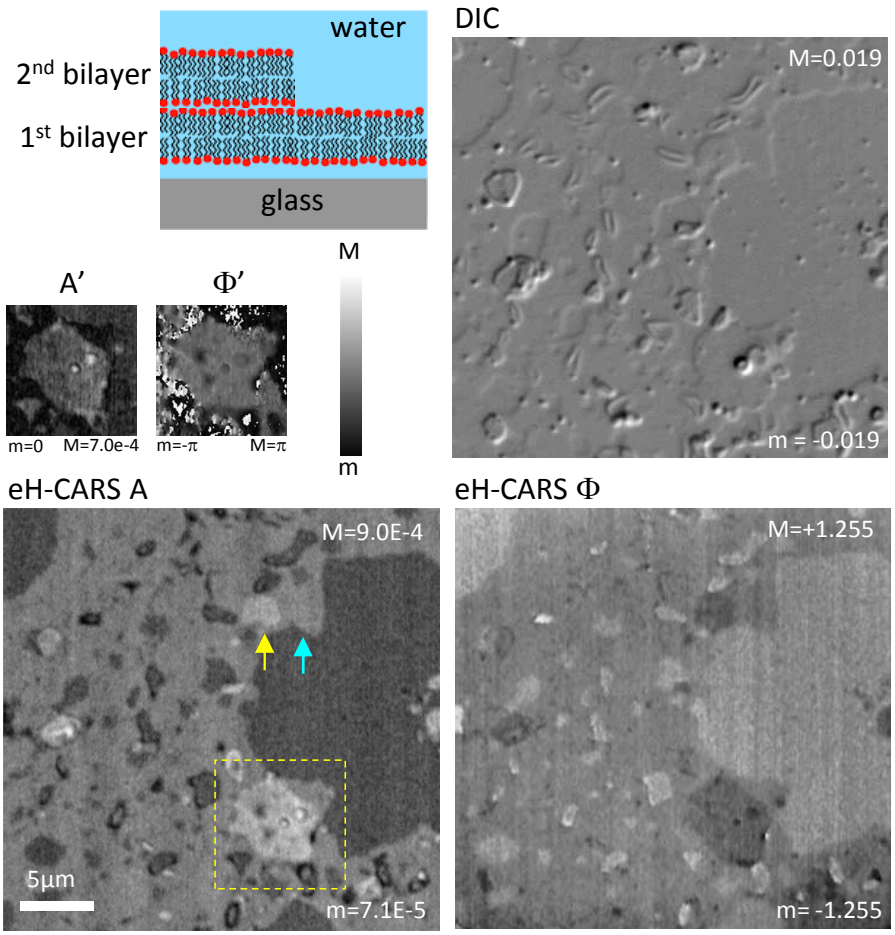

FIG. 7. Top left: Sketch of the sample made by spin coating and hydrating the lipid $DC_{15}PC$ onto a planar glass substrate in order to form regions with single and double bilayers. Top right: quantitative DIC image of the sample (differential phase δ, see text). Bottom: eH-CARS amplitude (A) and phase (Φ) of the same region measured at $2840\,\mathrm{cm}^{-1}$. The two arrows indicate steps going from the glass-water interface to a single bilayer (cyan arrow) and a double bilayer (yellow arrow). The insets A' and Φ' show amplitude and phase respectively from the regions indicated by the yellow dashed square, where the signal has been offset by the signal in the single bilayer regions, and phases are shifted to set the phase at the single bilayer to zero, for reference.

$\delta = \varphi_+ - \varphi_-$ with $\varphi_\pm = \varphi(\mathbf{r} \pm \mathbf{s}/2)$ being the optical phase accumulated in the sample for the beam passing through the point $\mathbf{r} \pm \mathbf{s}/2$ where $\mathbf{s}$ is the shear vector and $\mathbf{r}$ is the DIC image coordinate in the sample plane. We calculate δ using the exact analytical solution of the relationship between I_c and δ [25]. The image of δ is shown in Fig. 7(top right). The spatial distribution of the optical phase at the sample $\varphi(\mathbf{r})$ is then calculated from δ by performing a Wiener deconvolution procedure [34] (see also Sec. VII). Finally, the bilayer thickness can be calculated taking into account that the optical phase introduced by the lipid bilayer is $\varphi(\mathbf{r}) = 2\pi\Delta n t(\mathbf{r})/\lambda_0$ with the wavelength in vacuum λ_0, the refractive index change between the lipid bilayer and its surrounding aqueous medium Δn, and the thickness profile of the bilayer $t(\mathbf{r})$. Using $\Delta n = 0.1059$ (based on a refractive index of 1.44 for the $DC_{15}PC$ lipid [35], and 1.3341 for water) under the experimental condition $\lambda_0 = 647\,\mathrm{nm}$, we obtain the thickness profiles shown in Fig. 8 near the yellow and cyan arrows in Fig. 7. These profiles give a step height of about 5 nm for the region indicated by the cyan arrow, consistent with having a transition from the glass-water interface to a single lipid bilayer, and 11 nm for the region near the yellow arrow, consistent with a double bilayer step. Note that $DC_{15}PC$ is in the solid ordered (gel) phase at room temperature, which has a thickness

about 1 nm larger than a bilayer in the liquid disordered phase [36].

eH-CARS on the same region is shown in Fig. 7, measured at an IFD of $2840\,\mathrm{cm}^{-1}$, near the peak of the CH_2 symmetric stretch vibration of lipids and resolved in amplitude and phase as indicated. A clear contrast is obtained distinguishing regions with zero (0BL), one (1BL), and two (2BL) bilayers. The amplitude changes from 0BL to 1BL by a factor of about 1.6, corresponding to a CARS intensity change by a factor of about 2.6, which is slightly larger than the factor of 1.5-2 observed in intensity detected epi-CARS in Ref. 26. Line profiles corresponding to the DIC thickness profiles are shown in Fig. 8 as real and imaginary part of the eH-CARS field, deduced from the measured amplitude and phase, with a phase offset adjusted to provide a real field in the regions with zero bilayers, i.e. at the glass-water interface. To show the relative signal change due to the first and second bilayer, we normalize the complex signal by the 0BL signal, and show the result in the complex plane in Fig. 8(right). It is interesting to observe that the change due to the second bilayer, while having approximately the same amplitude as the change due to the first bilayer, shows a different phase. The green circles show the positions used to identify the signals from 1BL and 2BL, from which we find the change due to the first bilayer in amplitude and phase as $(0.6, -47°)$, and the change due to the second bilayer as $(0.5, -76°)$. The phase difference of 29° can be attributed to the sensitivity of the epi-detected signal phase on the axial position of the signal source, similar to what we recently showed by measuring the heterodyne epi-detected resonant four-wave mixing of single gold nanoparticles [37]. The phase slope can be estimated as $k_{\mathrm{signal}} + 2k_{\mathrm{Pump}} - k_{\mathrm{Stokes}}$ for plane wave excitation, resulting in $1.64°/\mathrm{nm}$, using the glass refractive index of 1.518, and the wavelengths 665 nm, 820 nm, 1069 nm for signal, Pump, and Stokes beam, respectively. The phase slope measured in the experiment by moving the sample was found to be $(1.4 \pm 0.2)°/\mathrm{nm}$, somewhat smaller than the above estimate as expected due to the Gouy phase shift in the focus. Using the measured phase slope, the observed phase difference corresponds to an axial position difference of 20 nm between first and second bilayer. Since the bilayer thickness is about 5 nm, as confirmed by the qDIC measurements, this suggests the presence of an additional water layer thickness of about 15 nm between the two bilayers in the investigated sample region. Furthermore, while the 1BL regions show a rather homogeneous signal, indicating that the first bilayer distance to the glass is well defined (and thus likely very short, below a few nanometers), 2BL regions show significant signal variations. This is specifically evident in the region indicated by the yellow square in Fig. 7. Since the bilayer thickness is expected to be well defined, these variations should be related to height variations. To follow this hypothesis, we show for this region A' and Φ', which are the amplitude and phase when using the signal of the 1BL region as offset and setting the phase offset to yield zero phase for the first bilayer signal. In this plot, we can see the 2BL region as a relatively homogeneous positive amplitude of about 0.25 mV, with a phase which is varying. In particular, we find two spots of about 70° reduced phase, corresponding to 50 nm axial position increase of the second bilayer, suggesting the formation of a "blister" in this region. These results exemplify the added capabilities of phase-sensitive eH-CARS compared to an intensity based detection, not only to distinguish and properly subtract non-resonant backgrounds, but also to extract additional information related to the topography of the sample. Note that, in general, without additional information, phase changes due to axial position changes cannot be separated from those due to susceptibility changes. However, this can be resolved by measuring at different IFDs. One could, for example, use an IFD for which it is known that the materials have a non-resonant response (for the lipid bilayers $2500\,\mathrm{cm}^{-1}$ for example), having a known phase of the material response, and thus determine the phase changes due to the axial position only. A more detailed study using the technique to study the biophysics of lipid bilayers is ongoing, and will be published elsewhere.

V. CONCLUSION

In summary, we have built and demonstrated a multimodal SRS/CARS microscope, featuring a novel dual polarization epi-heterodyne CARS with balanced diode detection, which

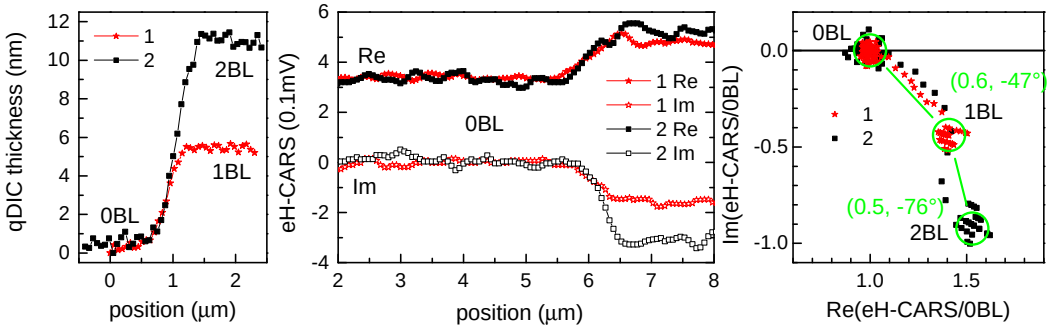

FIG. 8. Left: Thickness profile deduced from quantitative DIC analysis in regions near the yellow arrows in Fig. 7, showing a step going from the glass-water interface to a single bilayer (red) and to a double bilayer (black). Middle: Real (Re) and imaginary (Im) parts of the measured eH-CARS field along the same regions. Right: Imaginary versus real part, normalized to the signal at the zero bilayer. The data points for the zero, one and two bilayer regions are encircled (green).

offers background-free chemically-specific image contrast, shot-noise limited detection, and phase sensitivity. Through direct comparison on polystyrene beads in agar, we have shown that eH-CARS imaging is free from all the backgrounds and/or image artifacts limiting intensity-based forward CARS as well as SRS. The relevance of the phase-sensitive measurement is showcased on a planar single lipid bilayer, notoriously pushing CRS microscopy to its detection limits. Our results suggest that with this modality we not only can resolve a single lipid bilayer, distinct from a double bilayer, and measure the phase of its susceptibility, but also extract additional phase information to determine the topography of the bilayer with nanometer resolution.

As an outlook, this technique could prove instrumental when investigating the local field enhancement of CRS in the vicinity of a plasmonic nanostructure. The detection of such effect has proven to be challenging in the literature, due to the multiphoton fluorescence background and the instantaneous four-wave mixing arising from the metallic nanostructure itself[38,39]. Owing to the interferometric detection, our technique is free from fluorescence background and could distinguish CRS from instantaneous four-wave mixing via appropriate time-gating using the reference pulse. Thus our eH-CARS microscope set-up paves the way to exciting new experiments pushing the CRS sensitivity and resolution limits to the nanoscale.

The data presented in this work are available from the Cardiff University data archive[40].

VI. APPENDIX: METHODS

Experimental set-up. Optical pulses of 150 fs duration with $\nu_L = 80$ MHz repetition rate were provided by a Ti:Sa pulsed laser source (Mai-Tai HP, Spectra Physics) frequency-doubled to pump an Optical Parametric Oscillator (Inspire OPO, Radiantis). The idler of the OPO is used as Stokes beam, and is frequency shifted and amplitude modulated using an AOM (IntraAction ATM-781A2). The Stokes beam travels through a first glass block. Pump and Stokes travel through a second glass block and the various optics up to the sample. The resulting chirp provides a pulse duration around 1-2 ps. Furthermore, glass blocks were added to the reference beam path, starting from the signal beam of the OPO, in order to match the chirp of the CARS signal to maximize the interference between the epi-CARS and the reference field at the balanced detector. DBS1 (Melles Griot LWP-45-RP808-TP1064-PW-1025-C) recombined Pump and Stokes beams by transmitting wavelengths above 950 nm, and reflecting in the 780-870 nm range. DBS2 (Eksma optics, custom filter) transmitted Pump and Stokes beams in the 800-1200 nm range and reflected the CARS signal in the 620-715 nm range. The microscope objective was either a 60× magnification water-immersion objective of 1.27NA (Nikon CFI Plan Apochromat lambda-S, MRD07650),

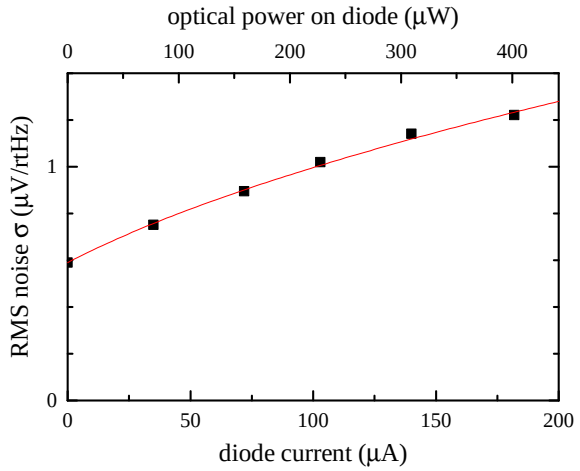

FIG. 9. RMS voltage noise σ of the balanced detector used for eH-CARS as function of reference power and corresponding photocurrent I per diode. The measured data are described well by $\sigma = \sigma_0\sqrt{1 + I/I_0}$, given by the red line, with $\sigma_0 = 0.59\,\mu$V/rtHz, and a shot noise equivalent current of $I_0 = 53\,\mu$A. Considering the amplifier transimpedance of 10^5 V/A, σ_0 corresponds to a current noise of 5.9 pA/rtHz, consistent with the expected current shot noise of $\sqrt{4eI_0} = 5.8$ pA/rtHz for a current of $2I_0$ from the diode pair.

for the measurements on polystyrene beads in agarose gel, or a 100× magnification oil-immersion objective of 1.45NA (Nikon CFI Plan Apochromat lambda, MRD01905), for the measurements on planar lipid bilayers, mounted into a commercial inverted microscope stand (Nikon Ti-U). The sample was positioned with respect to the focal volume of the objective by an xyz piezoelectric stage with nanometric position accuracy (MadCityLabs NanoLP200).

For SRS, the Stokes beam was amplitude modulated by the AOM, driven with a square wave amplitude modulation of frequency $\nu_\mathrm{m} = 2.5$ MHz, synchronized to the laser repetition rate to provide 16 pulses on followed by 16 pulses off. A small Gaussian beam waist $w_0 \approx 0.19$ mm was used in the AOM, to provide a rise time 10% to 90% of about 40 ns. F-CARS and SRS are collected by a 1.34 NA oil-immersion condenser in transmission geometry. A dichroic beamsplitter DBS3 (Semrock FF776-Di01-25x36, transmission > 776 nm) reflects the F-CARS signal and transmits the Pump and Stokes beams. F-CARS is spectrally selected by a band-pass filter F1 (stack of two Semrock FF01-675/67) and detected by a photomultiplier (Hamamatsu H10770A-40, 30% quantum efficiency at 660 nm). SRS in the form of stimulated Raman loss is measured at the Pump wavelength of 820 nm, seperated by the short-pass filter F2 (Semrock FF01-945/SP) from the Stokes beam. The SRS is detected as an intensity modulation at $\nu_\mathrm{m} = 2.5$ MHz via a PD (Hamamatsu S6976, 86% quantum efficiency at 820 nm) using a home-build resonant circuit at 2.5 MHz with a quality factor of 10 and 10 kOhm impedance at resonance (while having 3.6 Ohm DC impedance) and a local 10× voltage amplifier, analyzed by a dual phase lock-in amplifier (Zurich Instruments HF2LI) to take the in-phase (I) and in-quadrature (Q) components. A shot-noise limited detection is achieved for detected pump powers above 1 mW, limited by detector noise, and below 10 mW, limited by classical laser noise.

The dual polarization detector we use for eH-CARS is home-built with two pairs of balanced PDs (Hamamatsu S5973) of 85% quantum efficiency at 660 nm, a bandwidth of 5 MHz and a noise of each pair of 6 pA/rtHz at 3 MHz, equivalent to the shot noise of 112 μA photocurrent, corresponding to an incident optical power of 0.25 mW at a wavelength of 660 nm (see Fig. 9). In the experiment we use a reference power of about 1 mW per PD pair to reach a noise dominated by the reference shot noise. The amplifier has a transimpedance of 10^5 V/A and a high-frequency digital dual input dual-channel lock-in amplifier (Zurich Instruments HF2LI) was used to extract the eH-CARS signal. To provide the lock-in with an electronic reference for eH-CARS detection at $\nu_\mathrm{L} - \nu_\mathrm{s} = 3$ MHz, we assembled an electronic

circuit using coaxial BNC components (Minicircuits), mimicking the optical mixing, similar to what is described in Ref. 37.

The setup is controlled by home-built software written in Labwindows/CVI (National instruments), data acquisition boards (2 × National instruments PCIe-6353), and home-built electronics. The glass blocks are mounted on RC-servo actuated mounts, with lengths of 10, 20, 30, 40, and 80 mm, to enable adjustment of the glass length with 10 mm step size. The software calculates the group velocity dispersion, and selects the appropriate glass lengths to achieve similar chirp of Pump and Stokes beam, and a selectable spectral resolution by adjusting the chirp value. Pulse overlap and IFD calibration are calculated from the glass block settings and controlled using the delay lines (Physik Instrumente M-403.6DG with corner-cube retroreflectors).

F-CARS and SRS are acquired simultaneously, with modulation of the Stokes beam, which is required for SRS, but is reducing the CARS signal by a factor of two. eH-CARS is acquired separately (to avoid reflections of the reference beam at the CARS wavelength which interfere with the F-CARS signal) and without modulation.

The image data shown is obtained by mapping the measured time-traces of the signal using the measured position of the stage on the image grid using a Gaussian point-spread function (PSF) of 1.39 pixel full width at half maximum. This results in an averaging of the data of each pixel using all measurements within the PSF. For the phase, the wrap-around at $\pm\pi$ results for data dominated by noise in an averaging towards zero, which is visible in the reduced phase range of the noise regions compared to the full range $-\pi$ to π. In Fig. 6, the in-phase and in-quadrature components were separately mapped onto the image grid, and the amplitude and phase was determined for each pixel. When calculating the amplitude A from the in-phase (I) and in-quadrature (Q) component, we compensate for the RMS noise σ of each quadrature due to the detector using $A = \sqrt{I^2+Q^2} - s/(1+(I^2+Q^2)/s^2)$ with $s = 1.817\sigma$ to provide zero mean in the absence of signal.

In Fig. 2 the average Stokes power at the sample was 18 mW for eH-CARS and 9 mW for SRS and F-CARS due to the modulation. For the 3 μm and 1 μm diameter beads, the Pump power at the sample was 3.5 mW, pixel size was 70 nm in plane; for the 0.2 μm diameter beads, Pump power at the sample was 4.6 mW, pixel size was 50 nm in plane. For all data the pixel dwell time was 1 ms, and the axial steps were 200 nm. The data have been background subtracted using the signal for no pulse overlap (at an IFD of 2500 cm^{-1}) in the agar region as background. The Pump beam was centred at 820 nm and had 9.3 nm intensity FWHM. Propagation through 120 mm H-ZF52A resulted, including the group velocity dispersion of the other optics in the beam path, in a chirp of 102 $\mathrm{ps}^{-1}\mathrm{cm}^{-1}$ and 1.3 ps intensity FWHM pulse duration at the sample. The Stokes beam was centred at 1093 nm and had 15.7 nm intensity FWHM. Propagation through 220 mm H-ZF52A resulted in in a chirp of 120 $\mathrm{ps}^{-1}\mathrm{cm}^{-1}$ and 1.1 ps pulse duration at the sample. The mismatch of the chirp of about 18 $\mathrm{ps}^{-1}\mathrm{cm}^{-1}$over the pulse duration is smaller than the Fourier-limited FWHM of the excitation amplitude $\sqrt{S_F}$ (see Eq.(5) in Ref. 30) of 35 cm^{-1}. We quote here the FWHM in the amplitude since CRS is a coherent process. Using the power instead, the FWHM is a factor of $\sqrt{2}$ smaller, so 25 cm^{-1}. The reference beam was centred at 656 nm and had 6.1 nm intensity FWHM. Propagation through 100 mm H-ZF52A and 120 mm SF57 resulted in a chirp of 78 $\mathrm{ps}^{-1}\mathrm{cm}^{-1}$ and 1.8 ps pulse duration at the NPBS of the balanced detector. This matched the expected CARS chirp, taking into account the additional dispersion from the sample to the detector, within 7 $\mathrm{ps}^{-1}\mathrm{cm}^{-1}$, well below the Fourier-limited width and thus not significantly reducing the interference.

Data in Fig. 4 and Fig. 5 were taken using the same powers and pixel dwell time as in Fig. 2, and 50 nm pixel size. Data in Fig. 6 were taken using 7 mW Pump power, 32 mW Stokes power, 1 ms pixel dwell time, and 43 nm pixel size. Data in Fig. 7 were taken using the oil-immersion objective, 7 mW Pump power, 26 mW Stokes power, 63 nm pixel size, 0.5 ms pixel dwell time. The linear pulse chirp was 106 cm^{-1}/ps, with pulse durations (FWHM intensity) of 1.3 ps Pump and 1.7 ps Stokes, and a nominal spectral resolution of 28 cm^{-1}. We used 160mm (240mm) of H-ZF52A in Pump (Stokes), and 120mm SF57 and 50mm of H-ZF52A in the reference beam.

In the lipid bilayer data of Fig. 7, to suppress the influence of thermal drift and sample tilt

on the phase, we have applied a frequency high-pass filter to the detected signal phase, using a notch filter of Gaussian shape centred at zero frequency and with a standard deviation of 0.3 Hz. Furthermore, the phase slope by sample tilt was compensated using a notch filter of Gaussian shape at the fast axis scan frequency (2.1 Hz), with a standard deviation of 5 mHz. These filters were applied to the signal traces, before mapping them onto the image grid.

DIC was taken using the oil-immersion objective, and a 1.34NA oil condenser. Illumination was provided by a halogen tungsten lamp (V2-A LL 100W; Nikon), followed by a red filter (transmission 647 ± 35 nm; Semrock FF01-647/57) defining the wavelength range for the qDIC analysis. A de-Sénarmont compensator was used for offset phase adjustment (a rotatable linear polarizer followed by a fixed l/4 wave-plate, T-P2 DIC Polarizer HT; Nikon), followed by a Wollaston prism (T-C DIC Module High NA N2 Oil; Nikon) in the condenser unit, a Nomarski prism after the objective (D-C DIC Slider 100x; Nikon), and a linear polarizer (Ti-A-E DIC Analyzer Block; Nikon) in the filter turret. The corresponding shear distance was measured to be (238 ± 10) nm. DIC images were acquired using a scientific CMOS (PCO.edge 5.5; PCO, Germany) with 2560×2160 pixels of $6.5\,\mu$m size, a pixel full-well capacity of 30000 electrons, 0.54 electrons per count, and 16 bit digitization. For the measurements in Fig. 7 an exposure time of 5 ms was used for each frame in DIC images. The average over 256 frames was acquired with the angle of the de-Senarmont polariser set at $\pm 12.9°$. Home-built software written in Matlab was used to perform the qDIC integration.

Planar lipid bilayers. The supported lipid bilayer was prepared by spin coating, using a 24 x 24 mm Menzel Gläser (Braunschweig, Germany) glass coverslip as substrate. The coverslip was first cleaned by gentle wiping with acetone soaked lens paper, followed by "piranha" etching in a mixture of ACS grade sulfuric acid and hydrogen peroxide (30% in H_2O) in a 3:1 volumetric ratio at 95 °C for one hour. 1,2-dipentadecanoyl-*sn*-glycero-3-phosphocholine ($DC_{15}PC$) was purchased in powdered form from Avanti Polar Lipids (Alabaster, US) and used without further purification. The lipid was dissolved at 1 mg/ml in in 2-propanol. The glass coverslip was wetted with a volume of lipid solution sufficient to cover the entire coverslip, which was rotated at a speed of 3000 rpm for 30 s using a Laurell WS-650-23 spin coater, with 6 second acceleration and deceleration stages. All solvents were HPLC grade purchased from Sigma-Aldrich (St. Louis, US). After spin coating, the sample was subjected to a 60 minute pre-hydration process in which the coverslip was placed in a 50 ml centrifuge cylinder containing a small piece of tissue soaked in distilled water, at 37 °C. The cylinder was filled with nitrogen in order to prevent peroxidation of the lipids on the coverslip. The bilayer was then sealed into an enclosed chamber using a microscope slide and a Grace Bio-Labs (Bend, US) SecureSeal imaging spacer. The interior of the chamber was filled with PBS, which was degassed in vacuum for approximately five minutes immediately before use to reduce the formation of small air bubbles which can affect the DIC imaging.

VII. APPENDIX: QUANTITATIVE DIC ON PLANAR LIPID BILAYERS

As shown in Ref. 34 the transmitted intensity in a DIC microscope with de Sénarmont compensator can be expressed as

$$I_{\mathrm{out}}(\mathbf{r}, \psi) = \frac{I_{\mathrm{ex}}}{2} \left[1 - \cos\left(\psi - \delta(\mathbf{r})\right)\right], \tag{1}$$

with I_{ex} being the excitation intensity, $I_{\mathrm{out}}(\mathbf{r}, \psi)$ is the output intensity as a function of the position in the sample plain $\mathbf{r}$, ψ is the phase between the two linearly polarized components used in DIC, and $\delta(\mathbf{r})$ is the difference of the optical phase shift φ for the two beams that pass through the sample in two adjacent points separated by the shear vector $\mathbf{s}$

$$\delta(\mathbf{r}) = \phi(\mathbf{r} + \mathbf{s}/2) - \phi(\mathbf{r} - \mathbf{s}/2) \tag{2}$$

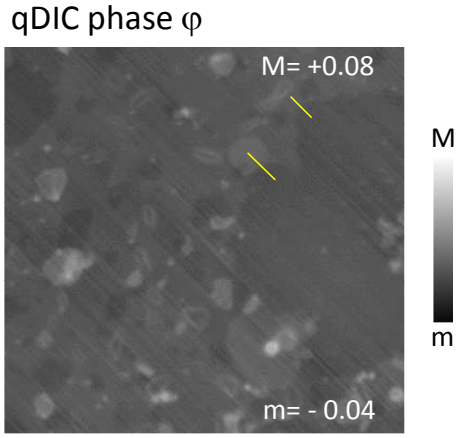

FIG. 10. Quantitative DIC image of the integrated optical phase φ measured on a $DC_{15}PC$ planar lipid bilayer, in the same region as shown in Fig. 7. Yellow lines show the line-cuts used for the qDIC thickness profiles in Fig. 8.

To reduce the influence of a possible spatial dependence of $I_{\rm ex}$ we acquire two images at opposite angles θ of the polarizer in the de Sénarmont compensator resulting in the output intensities [34] $I_\pm = I_{\rm out}(\mathbf{r}, \pm\psi)$ with $\psi = 2\theta$. The contrast image is then defined as

$$I_{\rm c}\left(\mathbf{r}\right) = \frac{I_+(\mathbf{r}) - I_-(\mathbf{r})}{I_+(\mathbf{r}) + I_-(\mathbf{r})}. \tag{3}$$

By combining Eq.(1) and Eq.(3), we obtain an expression that is independent of the local illumination intensity $I_{\rm ex}$

$$I_{\rm c}\left(\mathbf{r}\right) = -\frac{\sin(\psi)\sin(\delta)}{1-\cos(\psi)\cos(\delta)} \tag{4}$$

In Ref. 34 we used a linear approximation of this expression valid in the limit of $\delta \ll \psi < \pi$. On the other hand, equation Eq.(3) can be solved analytically without the requirement $\delta \ll \psi$, resulting in[25]:

$$\sin(\delta) = -I_{\rm c}\frac{1-\cos(\psi)\sqrt{1-I_{\rm c}^2}}{\sin(\psi)}\frac{1}{1+I_{\rm c}^2\cot^2\psi} \tag{5}$$

To retrieve the integrated phase φ, a Wiener deconvolution procedure was applied with the signal-to-noise parameter [34] $\kappa = 1000$. The resulting image is shown in Fig. 10 for the same region reported in Fig. 7. Yellow lines indicate the line-cuts used to determine the thickness profiles shown in Fig. 8 (left). The 'stripy' pattern along the shear direction is due to long-range integration artefacts which are significant for large κ, as discussed in Ref. 34, but the high value of κ is required to maintain the shape of the phase profile along the shear direction.

ACKNOWLEDGMENTS

This work was funded by the UK EPSRC Research Council (grant n. EP/I005072/1, EP/I016260/1, and EP/M028313/1) and by the EU (FP7 grant ITN-FINON 607842). P.B. acknowledges the Royal Society for her Wolfson Research Merit award (WM140077). Support of the development of the electronics by Rob Tucker and of the qDIC analysis by Joseph Williams are acknowledged.

[1]Zumbusch, A., Langbein, W. & Borri, P. Nonlinear vibrational microscopy applied to lipid biology. *Progress in Lipid Research* **52**, 615–632 (2013).
[2]Camp, C. H. & Cicerone, M. T. Chemically sensitive bioimaging with coherent raman scattering. *Nat. Phot.* **9**, 295–305 (2015).
[3]Liao, C.-S. & Cheng, J.-X. In situ and in vivo molecular analysis by coherent raman scattering microscopy. *Annu. Rev. Anal. Chem.* **9**, 69–93 (2016).
[4]Rinia, H. A., Burger, K. N. J., Bonn, M. & Müller, M. Quantitative label-free imaging of lipid composition and packing of individual cellular lipid droplets using multiplex cars microscopy. *Biophys. J.* **95**, 4908–4914 (2008).
[5]Masia, F., Glen, A., Stephens, P., Borri, P. & Langbein, W. Quantitative chemical imaging and unsupervised analysis using hyperspectral coherent anti-stokes raman scattering microscopy. *Anal. Chem.* **85**, 10820–10828 (2013).
[6]Camp, C. H. *et al.* High-speed coherent raman fingerprint imaging of biological tissues. *Nat. Phot.* **8**, 627–634 (2014).
[7]Napoli, C. D. *et al.* Hyperspectral and differential cars microscopy for quantitative chemical imaging in human adipocytes. *Biomed. Opt. Express* **5**, 1378–1390 (2014).
[8]Lu, F., Zheng, W. & Huang, Z. Elliptically polarized coherent anti-stokes raman scattering microscopy. *Opt. Lett.* **33**, 2842 (2008).
[9]Cheng, J.-x., Volkmer, A., Book, L. D. & Xie, X. S. An epi-detected coherent anti-stokes raman scattering (e-cars) microscope with high spectral resolution and high sensitivity. *J. Phys. Chem. B* **105**, 1277–1280 (2001). http://pubs.acs.org/doi/pdf/10.1021/jp003774a.
[10]Heinrich, C., Hofer, A., Ritsch, A., Christian Ciardi, a. B. & Ritsch-Marte, M. Selective imaging of saturated and unsaturated lipids by wide-field cars-microscopy. *Opt. Express* **16**, 2699 (2008).
[11]Pestov, D. *et al.* Optimizing the laser-pulse configuration for coherent raman spectroscopy. *Science* **316**, 265–268 (2007).
[12]Selm, R. *et al.* Ultrabroadband background-free coherent anti-stokes raman scattering microscopy based on a compact er:fiber laser system. *Opt. Lett.* **35**, 3282–3284 (2010).
[13]Rocha-Mendoza, I., Langbein, W., Watson, P. & Borri, P. Differential coherent anti-stokes raman scattering microscopy with linearly-chirped femtosecond laser pulses. *Opt. Lett.* **34**, 2258–2260 (2009).
[14]Rocha-Mendoza, I., Borri, P. & Langbein, W. Quadruplex cars micro-spectroscopy. *J. Raman Spectr.* **44**, 255–261 (2013).
[15]Ganikhanov, F., Evans, C. L., Saar, B. G. & Xie, X. S. High-sensitivity vibrational imaging with frequency modulation coherent anti-stokes raman scattering (FM CARS) microscopy. *Opt. Lett.* **31**, 1872–74 (2006).
[16]Evans, C. L., Potma, E. O. & Xie, X. S. Coherent anti-stokes raman scattering spectral interferometry: determination of the real and imaginary components of nonlinear susceptibility $\chi(3)$ for vibrational microscopy. *Opt. Lett.* **29**, 2923–2925 (2004).
[17]Potma, E. O., Evans, C. L. & Xie, X. S. Heterodyne coherent anti-stokes raman scattering (cars) imaging. *Opt. Lett.* **31**, 241–243 (2006).
[18]Jurna, M., Korterik, J. P., Otto, C., Herek, J. L. & Offerhaus, H. L. Vibrational phase contrast microscopy by use of coherent anti-stokes raman scattering. *Phys. Rev. Lett.* **103**, 043905 (2009).
[19]Freudiger, C. W. *et al.* Label-free biomedical imaging with high sensitivity by stimulated raman scattering microscopy. *Science* **322**, 1857 (2008).
[20]Saar, B. G. *et al.* Video-rate molecular imaging in vivo with stimulated raman scattering. *Science* **330**, 1368–1370 (2010). http://www.sciencemag.org/content/330/6009/1368.full.pdf.
[21]Ozeki, Y. *et al.* High-speed molecular spectral imaging of tissue with stimulated raman scattering. *Nature Photon.* **6**, 845–851 (2012).
[22]Berto, P., Andresen, E. R. & Rigneault, H. Background-free stimulated raman spectroscopy and microscopy. *Phys. Rev. Lett.* **112**, 053905 (2014).
[23]Freudiger, C. W. *et al.* Stimulated raman scattering microscopy with a robust fibre laser source. *Nat. Phot.* **8**, 153– (2014).
[24]Garbacik, E. T., Korterik, J. P., Otto, C., Herek, J. L. & Offerhaus, H. L. Epi-detection of vibrational phase contrast coherent anti-stokes raman scattering. *Opt. Lett.* **39**, 5814–5817 (2014).
[25]Pope, I. *et al.* Coherent anti-stokes raman scattering microscopy of single nanodiamonds. *Nat. Nanotech.* **9**, 940–946 (2014).
[26]Li, L. & Cheng, J.-X. Label-free coherent anti-stokes raman scattering imaging of coexisting lipid domains in single bilayers. *J. Phys. Chem. B* **112**, 1576–1579 (2008).
[27]Zoriniants, G., Masia, F., Giannakopoulou, N., Langbein, W. & Borri, P. Background-free 3d nanometric localization and sub-nm asymmetry detection of single plasmonic nanoparticles by four-wave mixing interferometry with optical vortices. *Phys. Rev. X* **7**, 041022 (2017).
[28]Rocha-Mendoza, I., Langbein, W. & Borri, P. Coherent anti-stokes raman microspectroscopy using spectral focusing with glass dispersion. *Appl. Phys. Lett.* **93**, 201103 (2008).
[29]Langbein, W., Rocha-Mendoza, I. & Borri, P. Single source coherent anti-stokes raman microspectroscopy using spectral focusing. *Appl. Phys. Lett.* **95**, 081109 (2009).
[30]Langbein, W., Rocha-Mendoza, I. & Borri, P. Coherent anti-stokes raman micro-spectroscopy using spectral focusing: Theory and experiment. *J. Raman Spectrosc.* **40**, 800–808 (2009).
[31]Karuna, A., Masia, F., Borri, P. & Langbein, W. Hyperspectral volumetric coherent anti-stokes raman scattering microscopy: quantitative volume determination and nacl as non-resonant standard. *J. Raman Spectrosc.* **47**, 1167–1173 (2016).

[32]Bagatolli, L. A., Ipsen, J. H., Simonsen, A. C. & Mouritsen, O. G. An outlook on organization of lipids in membranes: Searching for a realistic connection with the organization of biological membranes. *Prog. Lipid Res.* **49**, 378–389 (2010).
[33]Sezgin, E. *et al.* Partitioning, diffusion, and ligand binding of raft lipid analogs in model and cellular plasma membranes. *Biochimica et Biophysica Acta* **1818**, 1777–1784 (2012).
[34]McPhee, C. I., Zoriniants, G., Langbein, W. & Borri, P. Measuring the lamellarity of giant lipid vesicles with differential interference contrast microscopy. *Biophys. J.* **105**, 1414–1420 (2013).
[35]Howland, M. C., Szmodis, A. W., Sanii, B. & Parikh, A. N. Characterization of physical properties of supported phospholipid membranes using imaging ellipsometry at optical wavelengths. *Biophys. J.* **92**, 1306–1317 (2007).
[36]Leonenko, Z., Finot, E., Ma, H., Dahms, T. S. & Cramb, D. Investigation of temperature-induced phase transitions in dopc and dppc phospholipid bilayers using temperature-controlled scanning force microscopy. *Biophys. J.* **86**, 3783–3793 (2004).
[37]Zoriniants, G., Masia, F., Giannakopoulou, N., Langbein, W. & Borri, P. Background-free 3d nanometric localization and sub-nm asymmetry detection of single plasmonic nanoparticles by four-wave mixing interferometry with optical vortices. *Phys. Rev. X* **7**, 041022 (2017).
[38]Zhang, Y. *et al.* Coherent anti-stokes raman scattering with single-molecule sensitivity using a plasmonic fano resonance. *Nat. Comms.* **5**, 4424 (2014).
[39]Yampolsky, S. *et al.* Seeing a single molecule vibrate through timeresolved coherent anti-stokes raman scattering. *Nat. Phot.* **8**, 650–656 (2014).
[40]Cardiff University data archive: http://dx.doi.org/10.17035/d.2018.0046342430.